POLITECNICO DI TORINO
Repository ISTITUZIONALE

3D printing of dense and porous alkali-activated refractory wastes via Direct Ink Writing (DIW)

(Article begins on next page)

28 March 2024

3D printing of dense and porous alkali-activated refractory wastes via Direct Ink Writing (DIW)

Bartolomeo Coppola[a,*], Caroline Tardivat[b], Stéphane Richaud[b], Jean-Marc Tulliani[a], Laura Montanaro[a], Paola Palmero[a]

[a]Politecnico di Torino, Department of Applied Science and Technology, INSTM R.U. Lince Laboratory, Corso Duca Degli Abruzzi, 24, Italy

[b]LSFC Laboratoire de Synthèse et Fonctionnalisation des céramiques UMR 3080 CNRS / SAINT-GOBAIN CREE, SAINT-GOBAIN RESEARCH PROVENCE, 550 avenue Alphonse Jauffret, Cavaillon, France

[*]Corresponding author: bartolomeo.coppola@polito.it

Abstract

Alkali-activated pastes prepared starting from refractory wastes were successfully 3D-printed via Direct Ink Writing. In particular, as raw powders, two different aluminosilicates were used: chamotte (CH, mainly composed of corundum, mullite and andalusite) and alumina-zirconia-silica (AZS, mainly baddeleyite, corundum and amorphous silica). First, pastes rheological parameters were optimized in terms of liquid-to-solid ratio and polyethylene glycol content. Then, both dense prismatic samples and lattice structures were successfully 3D-printed. Additionally, PMMA beads of 20 and 60 μm diameter were used to generate an additional porosity in both dense and lattice structures, leading to hierarchically porous materials. Indeed, samples were partially sintered up to 800 °C, to decompose PMMA beads, when present, and provide very high mechanical properties: a flexural strength of approx. 45 MPa was obtained for both AZS and CH dense samples. Moreover, the addition of 30 vol% of PMMA beads leads to macroporous samples without affecting mechanical properties.

Keywords

Alkali-activation; Robocasting; 3D printing; Porous ceramics; Hierarchical Porosity

1. Introduction

Geopolymers, also referred to as inorganic polymers, and alkali-activated materials, have emerged as sustainable alternative to traditional Portland cement, having at the same time excellent mechanical strength, heat resistance and chemical inertness [1-4]. The feasibility to incorporate different industrial by-products (fly ash, metallurgical slag, glass waste, etc. [3-8]) into the raw materials has made the interest into geopolymers grow further, as a key model towards a circular and green economy. As a common feature, the above mentioned wastes are characterized by an aluminosilicate-rich composition, and an amorphous or poorly crystallized structure, which make them highly reactive under alkali-activation conditions, and therefore able to develop a significant strength in the hardened products [1-4].

Besides, the studies on highly porous geopolymer structures have exponentially increased in literature during the last few years, due to their remarkable properties in a number of applications. Specifically designed porous alkali-activated materials can be successfully used for thermal and acoustic insulation [9-11], lightweight construction materials [12-15], fire resistant materials [16-18], water and wastewater treatment [19-23], catalyst support [24-26], filtration membranes [27], dye removal [28] and plant cultivation systems [29].

A common and easy procedure to develop porous geopolymers consists on the addition of a foaming agent (such as hydrogen peroxide or fine metallic powder) to the fresh alkaline mixture [30,31]. By decomposition under the alkaline medium, gas bubbles are produced, and are then trapped inside the material during the setting and hardening stages. Direct foaming method can be used as well, where a surfactant is added to the slurry, which is then vigorously mixed to produce a large volume of voids in the specimens [32-36]. A further method implies the use of sacrificial pore formers (like polymer spheres), where the porosity is created by the extraction or thermal decomposition of the sacrificial template [37-40]. Finally, freeze casting technique [28], also known as ice-templating, allows to produce materials with aligned porosity [41]. The specimens are initially subjected to low temperatures to promote water freezing, and then in the second step (ice sublimation) water is removed from the samples, leaving behind unidirectional aligned pores.

Additive manufacturing (AM) opened the way to the fabrication of customized components, even with complex shapes, that traditional manufacturing techniques do not allow. The success of AM within all classes of materials, especially metals and polymers [42-44], paved the way for its exploitation even in the field of alkali-activated materials. In fact, AM is a very recent, and much less investigated, approach for producing geopolymers, where two main technologies are used: powder-based and extrusion-based methods. In the former approach, a liquid binder is jetted on a powder bed to make particles stick together [45-49]. Conversely, in extrusion-based processes, also known as direct inkjet writing (DIW) or robocasting, a delivery system (the extruder) accurately deposits precise amounts of paste over varying distances. Therefore, the slurry for the extrusion-based process should mainly meet two requirements: printability and buildability [50]. To comply with the first requirement, the paste must be flowable enough to be easily deposited without plugging the nozzle, and to produce continuous filaments. Buildability, on the other hand, is the ability of the freshly extruded layer to sustain the load before the subsequent layer falls over it [51]. Ideally, ceramic pastes suitable for DIW should behave like Bingham pseudoplastic fluids, i.e. they show an initial yield stress, and, once the yield stress is exceeded, they show a shear thinning behaviour at increasing shear rates.

Extrusion-based processes have been successfully used to fabricate dense [52-63] and lattice structures [22,24,64,65], being in this last case the shape retention (i.e. the preservation of the filamentary shape after extrusion) and the ability of suspended filaments to stand under their own weight the keys for a successful fabrication. Just few previous papers [52,65] investigated the possibility to prepare microporous geopolymer structures by AM. Agnoli et al. [52] developed metakaolin-based geopolymers by extrusion-based method. The addition of microalgal biomass in the formulation firstly allowed to partially fill the starting high porosity (around 70%); then, the following thermal decomposition at 800°C, allowed to produce samples with around 30% porosity and high mechanical strength. Alghamdi et Neithalath [65] developed lattice structures, still by extrusion process, by also adding a surfactant to the fly-ash based formulation. Dual-porosity structures, with porosities ranging from 55 to 75% and bimodal pore size distribution (0.3-0.8 µm and 20-100 µm) were successfully printed, providing innovative thermal insulation prototypes.

In this work, different architectures (dense, lattice, microporous and dual-porosity structures) have been developed by DIW fabrication method. As compared to previous literature, different points of innovation are here proposed. First, the authors have exploited their know-how dealing with the development of high-strength alkali-activated materials by using highly crystalline, mineral waste powders. Thanks to such innovative approach, wastes derived by ornamental stone production [66-68], construction and demolition activities [69,70], and refractory products [71] were used to fabricate new alkali-activated materials by traditional casting process. In particular way, in a recent publication [71] the feasibility to prepare alkali-activated materials starting from alumina-zirconia-silica (AZS) and mullite-corundum-andalusite (chamotte, CH) fine wastes, able to withstand very high temperatures (up to 1400 °C) was demonstrated and a certain reactivity between raw powders and alkaline solution was demonstrated using XRD and FT-IR techniques [71]. These fines were mixed with an alkaline aqueous solution of sodium hydroxide and sodium silicate, achieving very high mechanical properties (compressive strength of 60 and 70 MPa for AZS and CH pastes, respectively), which further increased after firing at high-temperatures. CH achieved compressive strength values of more than 180 MPa by firing at 800°C; AZS reached about 120 MPa after the same calcination treatment, and achieved ~ 180 MPa after firing in the 1200-1400°C range.

In this work, the same waste-based formulations were further optimized and engineered to produce 3D printable slurries. To the best of the authors' knowledge, for the first time mineral-based alkali-activated pastes have been successfully printed in the form of fully dense and lattice structures. As a further innovation, microporous and dual-porosity structures were developed as well, by joining the sacrificial template method to the DIW process. In fact, polymethyl methacrylate (PMMA) fine spheres were added to the slurry, to develop a controlled porosity in both fully dense and lattice specimens. PMMA spheres (having different diameters, i.e. 20 and 60 μm) were mixed with the fresh pastes by further optimizing their rheological behaviour. Samples were calcined at 800°C, in order to decompose the sacrificial spheres, and simultaneously reach very high mechanical strength.

2. Experimental

2.1 Materials

Alkali-activated pastes were prepared starting from two powders, representative of a typical waste resulting from the recycling of used refractory materials: chamotte (CH) and alumina-zirconia-silica (AZS), both provided by Saint-Gobain Research Provence (Cavaillon, France). In a previous work [71], the same powders were comprehensively characterized in terms of particle size, crystalline phases composition and thermal stability. AZS (ρ = 3.75 g/cm^3) is a typical refractory used in glass furnaces, obtained by electrofusion, mainly composed of corundum (α-Al$_2$O$_3$) and monoclinic ZrO$_2$ (baddeleyite). CH (ρ = 3.00 g/cm^3) is a refractory material mainly composed of andalusite (Al$_2$SiO$_5$), mullite (Al$_6$O$_{13}$Si$_2$) and corundum, obtained by shaping and sintering. Both samples were provided as ground powders having a d$_{50}$ (i.e. the particle size at 50% of the cumulative distribution) of 6.25 and 4.66 µm, for AZS and CH respectively [71]. Both AZS and CH powders are characterized by irregular particles (Figure 1 and Figure 2, respectively) due to the grinding process. Moreover, AZS contains more fines (d < 0.5 µm) compared to CH [71].

The alkaline activating solution was prepared using sodium hydroxide (NaOH, purity > 98%, pellets, Sigma Aldrich), sodium silicate solution (ρ = 1.35 g/cm^3, pH 11.0-11.5, SiO$_2$ = 25.5-28.5% and Na$_2$O = 7.5-8.5%, Sigma Aldrich) and distilled water. Polyethylene Glycol (PEG) in pellets form (M$_w$ = 2000, pH = 4-7, ρ = 1.21 g/cm^3, Sigma-Aldrich) was used in some formulations to modify pastes rheological properties.

Poly(methyl methacrylate) (PMMA) spheres (Microbeads AS) of 20 and 60 µm diameter (Figure 3) were used as fugitive phase for the preparation of porous samples.
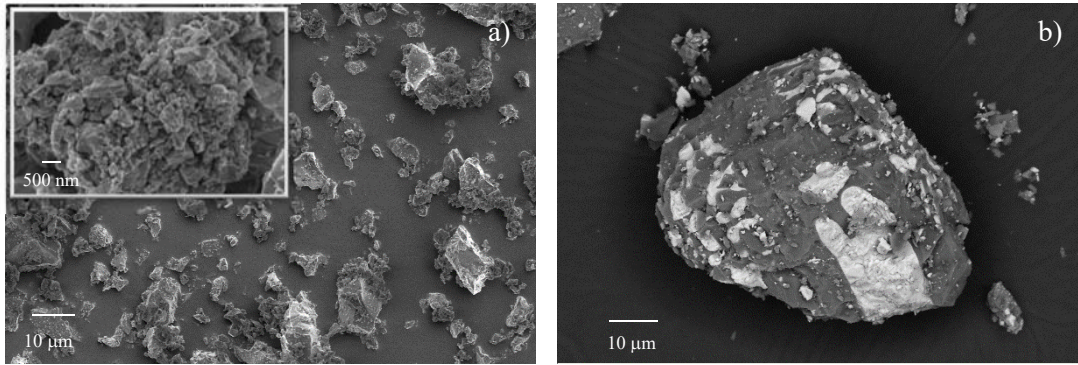
Figure 1: AZS powder at different magnifications a) and b) BSE micrograph (reprinted from [71], license 4844670457969)
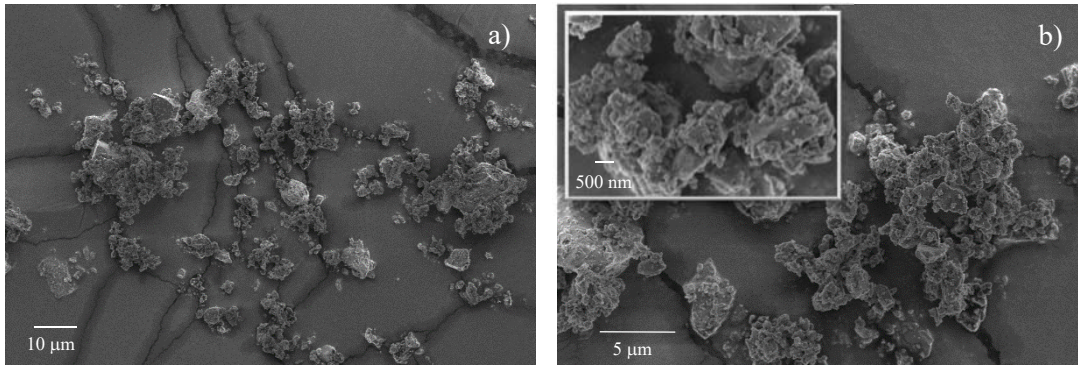

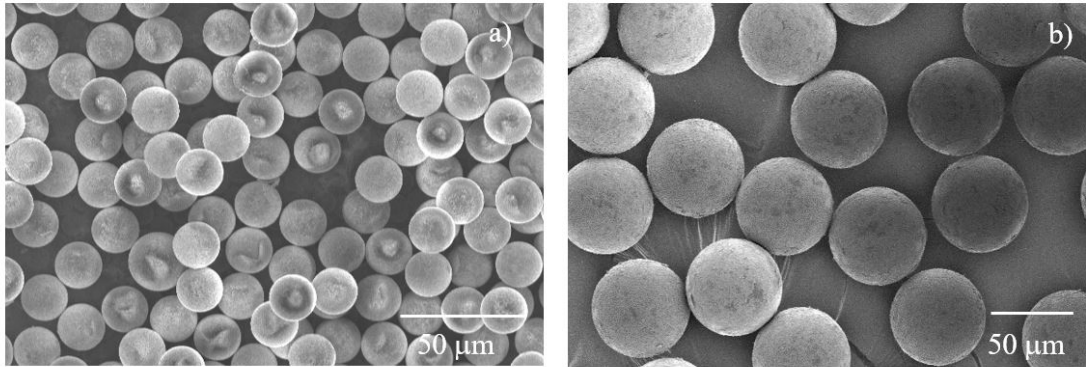**Figure 2:** CH powder at different magnifications (reprinted from [71], license 4844670457969)

Figure 3: PMMA spheres of a) 20 μm and b) 60 μm diameter

2.2 Alkali-activated pastes preparation

To understand the printability range of alkali-activated refractory waste pastes, numerous formulations were explored. The alkaline solution made of sodium hydroxide, sodium silicate and distilled water (NaOH, Na_2SiO_3 and H_2O respectively) was prepared at fixed SiO_2/Na_2O molar ratio (i.e. 1.65, corresponding to 14% Na_2O, 23% SiO_2 and 63% H_2O) as determined in previous studies [66,67,71]. First, NaOH pellets were

7

dissolved in distilled water under continuous stirring for 2 hours then, sodium silicate was added and the stirring was continued for two further hours. Pastes were prepared by mixing refractory waste powders (i.e. CH or AZS) for 5 minutes in a vacuum mixer (D-VM 16, Harnisch+Rieth, Germany). Different liquid to solid volume ratios (L/S), considering as liquid the solution made of water, sodium hydroxide and sodium silicate, were investigated (Table 1), to first determine the printability range via rheological measurements and then to print samples via robocasting. In some cases, it was necessary to add a low molecular weight PEG, at different wt% respect to the activating solution, to modify pastes rheological properties (Table 1). For such pastes, PEG pellets were dissolved in the activating solution before powder addition. Finally, in some formulations, 30 vol% PMMA spheres were added, too, to obtain microporous samples, by opportunely tuning L/S (Table 1). For sake of clarity, samples designation and composition are reported in Table 1. For example, AZS_47/53-13PEG (60) is the sample made of AZS with a L/S of 47/53, containing 13 wt% of PEG and 30 vol% of PMMA spheres having a diameter of 60 μm. The last column of Table 1 provides the optimized formulations that were successfully 3D printed and characterized.

2.4 Pastes rheological properties

Alkali-activated pastes rheological properties were determined using a rotational rheometer (Kinexus, Malvern, UK) equipped with parallel plates (diameter 20 mm) having a gap of 1 mm. Both the upper and the lower plate were sandblasted to avoid paste slipping. During the tests, the temperature was kept constant at 20 ± 0.05 °C thanks to a heat-exchanger system. A water-moisture solvent trap was used to minimize paste evaporation during rheological tests. Steady rate sweep tests were carried out with a shear rate increasing from 0.01 to 100 s^{-1} at a frequency of 1 Hz. The measurements were done immediately after pastes preparation on at least three different samples.

Table 1: Designation and composition of the alkali-activated pastes.

Sample name	Refractory powder	Liquid/Solid	PEG° (wt%)	PMMA spheres		3D printed
				vol%^	Diameter (μm)	
CH_35/65	Chamotte	35/65	-	-	-	-
CH_38/62	Chamotte	38/62	-	-	-	X
CH_40/60	Chamotte	40/60	-	-	-	-
AZS_39/61	AZS	39/61	-	-	-	-
AZS_41/59	AZS	41/59	-	-	-	-
AZS_43/57	AZS	43/57	-	-	-	-
AZS_41/59-6.5PEG	AZS	41/59	6.5	-	-	-
AZS_41/59-13PEG	AZS	41/59	13	-	-	X
AZS_47/53 -13PEG (60)	AZS	47/53	13	30	60	-
AZS_47/53-5PEG (60)	AZS	47/53	5	30	60	X
AZS_50/50-5PEG (60/20)	AZS	50/50	5	30	60/20	X
CH_43/57 (60)	Chamotte	43/57	-	30	60	X
CH_45/55 (60/20)	Chamotte	45/55	-	30	60/20	X

° relative to the activating solution

^ relative to the volume of the paste

2.4 3D printing

Alkali-activated pastes were 3D printed via Direct Ink Writing (DIW) using a Nordson SL940 slurry deposition system, used also in a previous work to print Boehmite suspensions [72]. After mixing, pastes were poured into plastic syringes (30 cc, Nordson Corporation) equipped with a conical nozzle having a diameter of 840 μm (Poly Dispensing Systems). The printing head containing the syringe moves along programmed X-Y and Z axes, dispensing the paste through an air pressure-driven plunger. All the specimens were printed on microscope glass slides at ambient temperature. Prismatic samples measuring $50 \times 5.88 \times 5.04$ mm^3 (Figure 4a) were printed for three-point bending tests. Lattice structures ($21 \times 20 \times 6.72$ mm^3) having several infills (25, 50 and 75%, respectively) were printed to investigate the feasibility to print self-standing complex structures (Figure 4b).
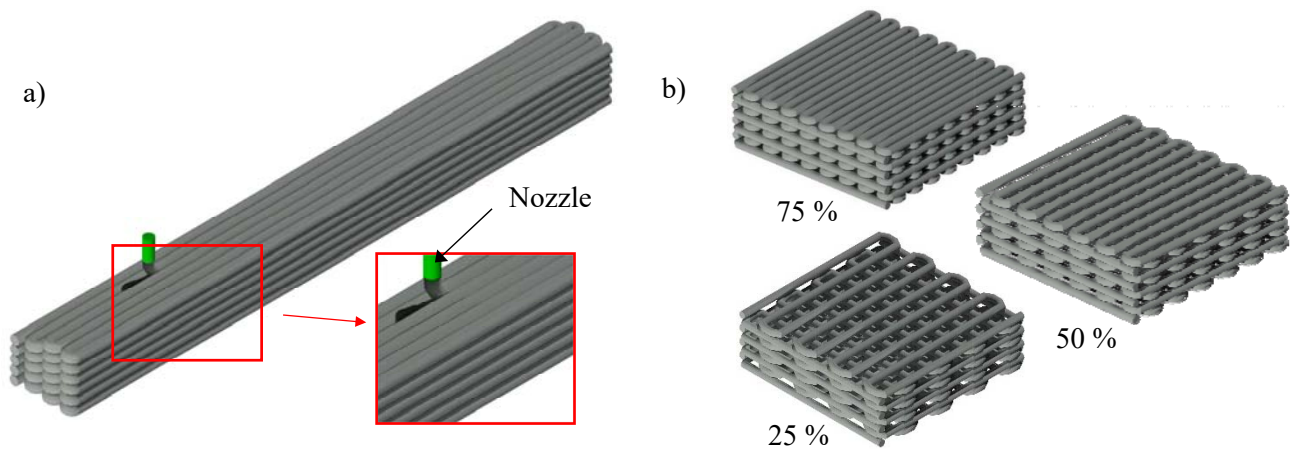
Figure 4: CAD models and schematic representation of the 3D printing process for a) prismatic samples and b) lattice structures

After printing, samples were oven-cured for 24 hours at 60 °C in sealed vessels. Then, samples were stored in closed containers for 28 days at constant relative humidity and temperature (RH=95 ± 2 % and 20 ± 3 °C, respectively) before high-temperature exposure. 3D printed samples, both containing or not PMMA spheres, were heated at 2°C/min up to 800 °C in an electric furnace (Nabertherm GmbH, Germany) according to the thermal cycle reported in Figure 5. This heating cycle was used both to decompose PMMA spheres (thermal degradation of PMMA under air is accomplished around 400 °C [73]) without damaging 3D printed samples, according to previous studies [37,38], and to partially sinter the alkali-activated samples, as discussed in a previous work [71]. Then, specimens were left in the furnace to cool down gradually to room temperature.
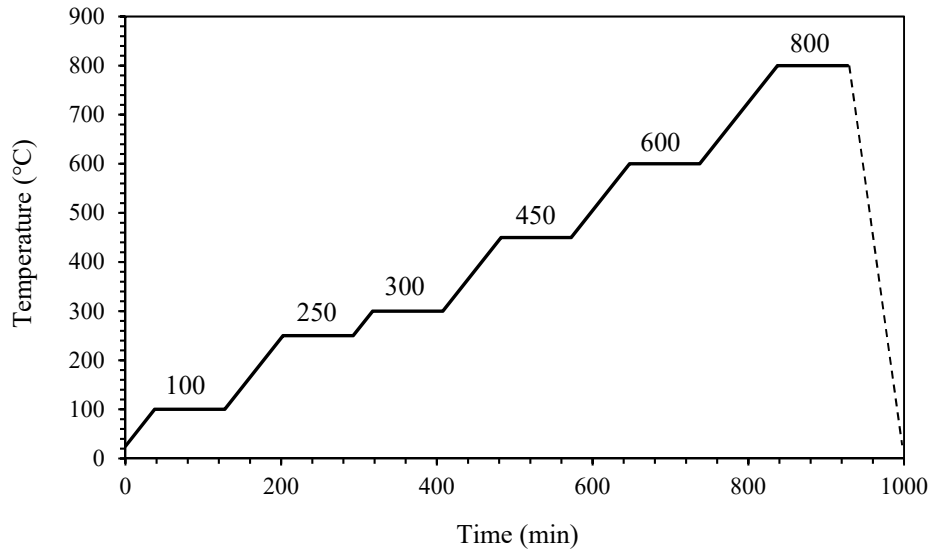
Figure 5: Thermal cycle used for 3D printed CH and AZS pastes (heating rate 2°C/min, dwells 90 min)

2.5 Samples characterization

Mechanical properties of 3D printed dense and microporous prismatic samples (Figure 4a) were determined using an electromechanical testing system (Zwick Roell 2014, Ulm, Germany) equipped with a load cell of 50 kN. Three-point bending flexural strength was determined in displacement control mode applying the load with a crosshead rate of 0.5 mm/min and a span of 20 mm. At least three samples were tested for each composition.

The pore size and the pore size distribution of dense and microporous 3D printed alkali-activated materials were investigated via Mercury Intrusion Porosimetry (MIP) using an AutoPore IV 9500 mercury porosimeter (Micromeritics, Georgia, USA) from pressure 0.07 to 413.69 MPa. At least three measurements were carried out for each composition.

Morphology of dense, microporous and micro/macroporous 3D printed samples were examined by means of a FE-SEM (Zeiss Supra-40, Oberkochen, Germany) equipped with an Oxford Energy Dispersive X-ray detector. The observations were performed on polished surfaces, coated with a thin chromium layer.

11

3. Results and Discussion

3.1 Rheological properties and printability

Pastes rheology is a key factor in the DIW process, particularly for complex shapes with unsupported parts (such as lattice structures). Moreover, pastes rheology is fundamental to avoid nozzle clogging or printing defects. Therefore, one of the most important rheological parameters is the shear viscosity (η): during the extrusion, i.e. at high shear rates, η should be sufficiently low to allow the extrusion; conversely, once the filament is deposited, i.e. at zero shear, η should be high enough to avoid filament deflection.

In Figure 6, the flow curves of CH pastes prepared at different L/S (i.e. 35/65, 38/62 and 40/60, respectively) are depicted. As expected, the higher the solid content, the higher the shear viscosity. In particular, at low shear rates, a moderate increase of shear viscosity was observed moving from CH_40/60 to CH_38/62, and a sharp increase was observed by further moving to CH_35/65 (Figure 6). All the investigated pastes, independently on their L/S, displayed a shear thinning behaviour (i.e. a decrease of shear viscosity at increasing shear rates, as required to achieve a good printability), which was more pronounced for the CH_35/65 paste.
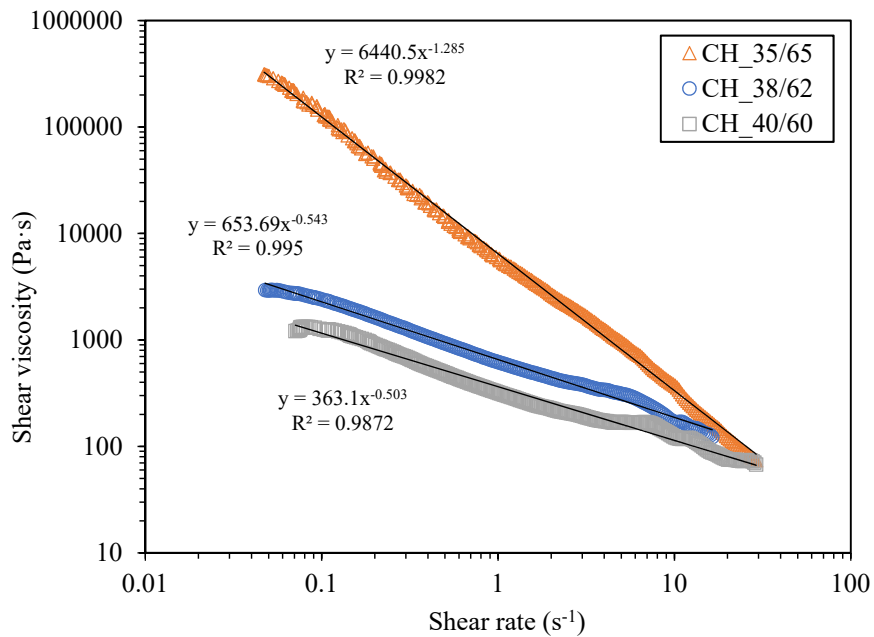

Figure 6: Flow curves of CH pastes at different L/S (i.e. 35/65, 38/62 and 40/60, respectively)

In the case of AZS pastes, the flow curves at different L/S are depicted in Figure 7. As in the previous case, all the investigated AZS pastes present a shear thinning behaviour with a moderate increase of the viscosity by decreasing L/S. However, the flow curves of AZS pastes approximately run parallel, contrary to the previous case (Figure 6). Moreover, to obtain a similar shear viscosity, AZS pastes should have a higher L/S compared to CH pastes, as we can observe by comparing AZS_41/59 with CH_38/62, being this behaviour already assessed in a previous work [71] and probably due to the presence of more fines.
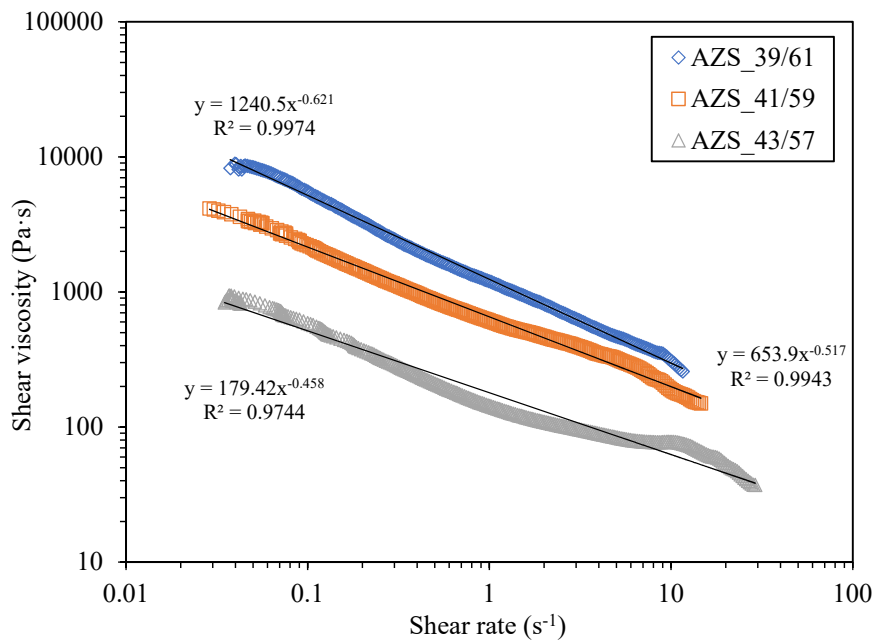

Figure 7: Flow curves of AZS pastes at different L/S (i.e. 39/61, 41/59 and 43/57, respectively)

Once defined the rheological behaviour, preliminary printing tests were carried out with all the above mentioned alkali-activated pastes. Printability was evaluated through the extrusion regularity, meaning the possibility to print two consecutive layers without nozzle clogging or printing defects. Several printing tests were carried out, by optimizing the key parameters such as printing speed and air pressure in the syringe. Moreover, considering that the extrusion process is the flow of a viscous fluid (i.e. the alkali-activated paste) through the nozzle, the shear rate applied to the paste can be calculated as:

$$\dot{\gamma} = \frac{4Q}{\pi r^3} \qquad \text{(eq. 1)}$$

where $\dot{\gamma}$ is the shear rate, Q is the volumetric flow rate and r is the radius of the nozzle. Starting from eq. 1 and considering the printing parameters used for both AZS and CH pastes, the shear rate in the DIW process was approx. between 8 and 12 s^{-1}. Thus, the viscosity at 10 s^{-1} (η_{10}) was considered as reference value to compare printability of the different alkali-activated pastes (Figure 8). As evident, a clear linear relationship exists between viscosity at 10 s^{-1} and the L/S ratio.

In both cases, pastes with the lowest investigated L/S (i.e. CH_35/65 and AZS_39/61) were too viscous to be printed. It means that with the highest achievable air pressure in the syringe (approx. 6 bar) it was impossible to extrude the pastes. On the contrary, pastes with the highest investigated L/S (i.e. CH_40/60 and AZS_43/57) were too fluid and pastes were leaked out from the nozzle even without applying any pressure in the syringe. As stated before, and also well evidenced by Figure 8, at fixed η_{10} values, printable AZS pastes have higher L/S compared to CH pastes. Moreover, AZS pastes printability range is narrower, in terms of L/S and thus viscosity, compared to CH pastes. The best formulations in terms of printability were AZS_41/59 and CH_38/62 pastes, characterized by a η_{10} viscosity of approx. 200 Pa·s.
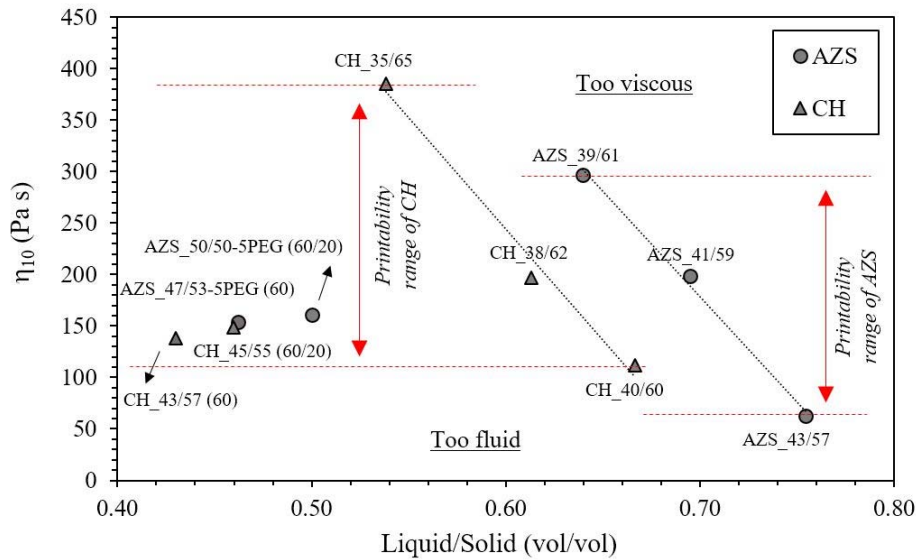

Figure 8: Printability range and viscosity at 10 s^{-1} (η_{10}) for different AZS and CH pastes, as a function of L/S

However, once set the printable formulation range for both compositions, a further optimization was required in the case of AZS. In fact, AZS_41/59 formulation was further modified to avoid the coalescence of extruded filaments, occurring few seconds after printing (Figure 9a). This issue was overcome adding a certain amount of PEG to the formulation (precisely, 6.5% and 13.0% as respect to the activating solution, as shown in Table 1). Shape retention was successfully improved by PEG addition, at both concentrations, as it acted as rheology modifier, as clearly shown in Figure 9. Indeed, while the PEG-free sample (AZS_41/59 without PEG) showed a significant coalescence between the extruded filaments (Figure 9a), in the modified formulation (AZS_41/59-13PEG), the individual printed filaments can be easily recognized (Figure 9b).
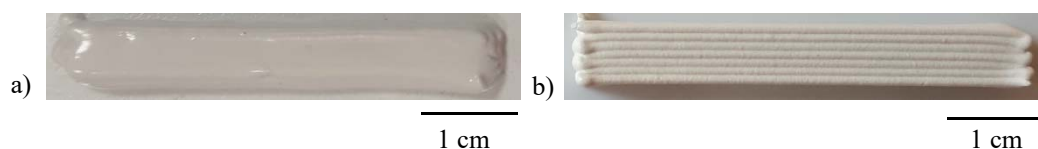

a)   b)

1 cm   1 cm

Figure 9: Digital photographs showing: a) filaments coalescence occurring in AZS_41/59 printed paste and b) AZS_41/59-13PEG prismatic sample in which this defect was overcome

Flow curves of AZS pastes with different PEG amounts were investigated and reported in Figure 10. Compared to the AZS_41/59 paste, PEG addition increases viscosity at low shear rates while promotes the shear thinning behaviour at increasing shear rates, particularly for the highest investigated PEG amount (13 wt%). The role of PEG is to promote shear thinning behaviour during the extrusion process and to confer a rapid viscosity recover at zero shear, i.e. after printing. Comparing η_{10} values, AZS_41/59-13PEG paste is less viscous than AZS_41/59 one (113 Pa·s and 199 Pa·s, respectively) but significantly more viscous than AZS_43/57 paste (62 Pa·s).
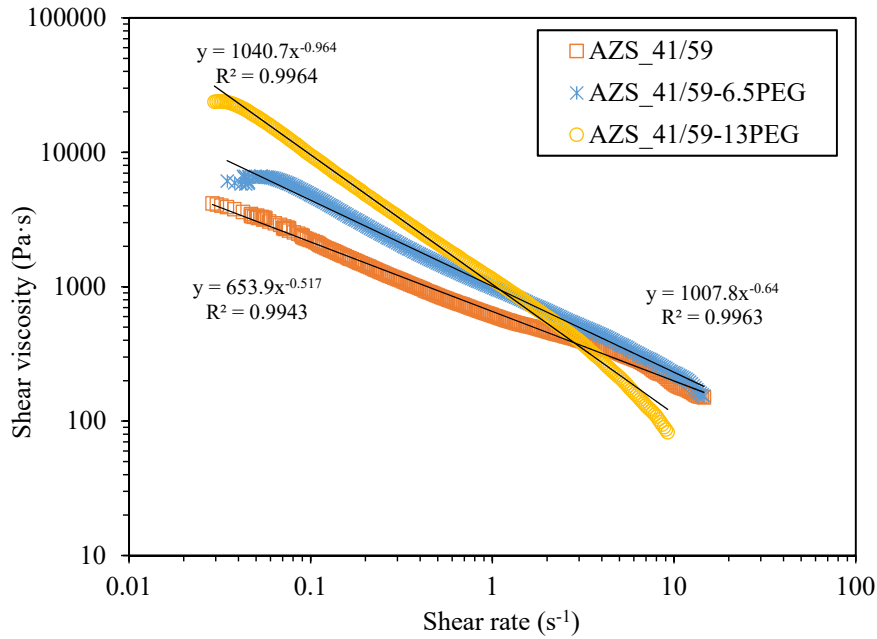
Figure 10: Flow curves of AZS pastes containing different PEG amounts (0, 6.5 and 13 %, respectively)

Finally, the last step was PMMA spheres addition for the preparation of microporous samples. Once again, it

was necessary to modify pastes formulation (Table 1) to allow the printability of alkali-activated pastes

containing PMMA spheres. As a matter of fact, PMMA spheres addition lead to a viscosity increase, due to

the overall increase of solid matter (powder + solid spheres) in the formulations. In addition, even if PMMA

spheres are perfectly spherical (Figure 3), a certain viscosity increase due to the friction between spheres and

irregular particles of AZS (Figure 1) and CH (Figure 2) can be postulated. To satisfy the printability

conditions, it was therefore necessary to add an extra amount of liquid, leading to an increase of L/S ratios

for both AZS and CH pastes. Moreover, the presence of smaller PMMA spheres (20 μm-diameter) in alkali-

activated pastes required a further increase of the liquid content (Table 1). Therefore, the L/S for CH pastes

was increased from 38/62 to 43/57 and 45/55 for CH pastes with 60 μm spheres and mixed 60/20 μm

spheres, respectively. On the other side, for AZS pastes, L/S was modified from the starting 41/59 value to

47/53 and 50/50 ratios for AZS pastes with 60 μm spheres and mixed 60/20 μm spheres, respectively.

Considering PMMA spheres as solid content, the achieved viscosities perfectly fulfilled the printability range

highlighted in Figure 8. Moreover, a variation of the PEG amount was also necessary for AZS pastes

containing PMMA spheres (Table 1). In particular, PEG quantity was decreased from 13 to 5vol% to

improve spheres dispersion in the AZS paste (Figure 11). In fact, even if AZS_47/53-13PEG (60) satisfied the printability conditions, a certain extent of spheres agglomeration was observed by optical microscopy (Figure 11a). On the contrary, upon PEG reduction, not only spheres dispersion was improved, but also shape retention, as evident from the ease of recognition of the deposited paste filaments (Figure 11b).
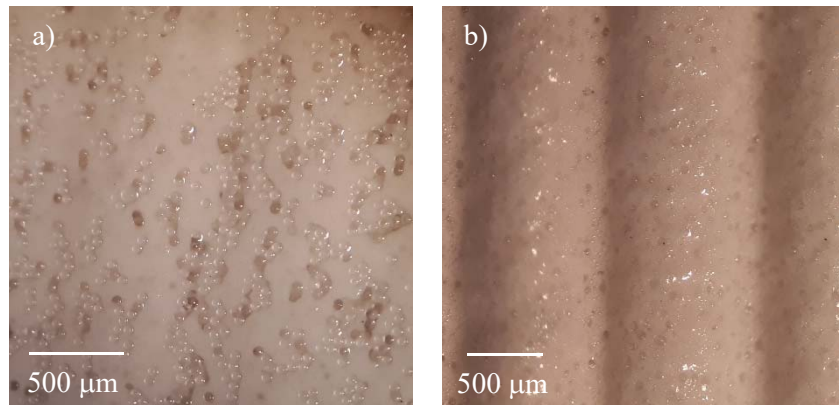

Figure 11: Optical microscope images of a) AZS_47/53-13PEG (60) and b) AZS_47/53-5PEG (60)

3.2 Physical and mechanical properties

The optimization of the fresh properties allowed the successful printing of dense and porous AZS and CH specimens. The physical (density and porosity) and mechanical properties (bending strength) of the printed prismatic samples were correlated in Figure 12 and Figure 14. Density was measured both via Archimedes' method and MIP (bulk density). The values obtained with the two methods were almost the same.

In Figure 12, CH samples showed a progressive decrease of the density moving from the dense specimen (2.41 g/cm^3), to the CH_43/57 (60) porous sample (1.76 g/cm^3), to the CH_45/55 (60/20) one (1.52 g/cm^3). The former reduction was in line with the expected variation due to the 30vol% added porosity. The latter can be reasonably justified by the higher water release from the sample at higher L/S.

In the case of AZS samples, a certain reduction moving from the dense specimen (2.34 g/cm^3) to the porous AZS_47/53-5PEG (60) one (2.01 g/cm^3) was observed, too, but lower than the expected one due to PMMA beads addition. In addition AZS_50/50-5PEG (60/20) samples showed a similar density (2.22 g/cm^3) to the dense one. For AZS materials, a clear correlation between the density and the added spheres cannot be established, as differences in water and PEG amounts among the three compositions exists.

Figure 12 indicates a clear linear relationship between bending strength and samples density. Bending strength of dense samples (both AZS and CH) is approx. 45 MPa, coherently to what obtained in a previous work [71] where bending strengths of AZS and CH cast materials, after exposure to 800 °C, were 32 and 38 MPa, respectively. Interestingly, bending strength of 3D printed samples is higher than that of traditionally cast samples, even if L/S ratios of 3D printed samples are slightly higher compared to those used in the above-mentioned work (35/65 and 38/62 for CH and AZS-based pastes [71], respectively). However, a direct comparison cannot be done but this result is representative of a good printing process. Indeed, one of the main concerns is related to the low mechanical properties of 3D printed parts, due to the lack of adhesion between layers or to the anisotropic mechanical response [53,54,57,62]. To overcome this drawback, some authors investigated the possibility to reinforce geopolymeric pastes with fibers [60,61] or fillers [57-59,63], similarly to cement technology [74,75].

In this work, outstanding mechanical properties were achieved for dense and porous samples can be imputed to both the optimization of printable slurry and the firing at 800 °C. It is worth mentioning that, in spite the expected decrease in the porous samples, very high flexural strength values, in the range 20-30 MPa, were obtained, too. Alghamdi et al. [58] reported flexural strengths of 3D-printed alkali activated fly ash-based binders ranging between 1 and 4.5 MPa. Bong et al. [62] reported a different flexural strength considering perpendicular or lateral testing (7.1 and 6.3 MPa, respectively) due to 3D-printed object anisotropy. Agnoli et al. [52] reported a compressive strength in the range 20-45 MPa for metakaolin-biomass mixtures printed by an extrusion-based method and fired at 800 °C, providing a porosity ranging from ~ 30 to 50%. However, no flexural strength values, for a more direct comparison, were determined.

Comparing the trends of AZS and CH samples, the former showed a steeper decrease of the strength as a function of the density, compared to the latter. However, the lowest value were those measured for CH porous samples containing both 60 and 20 μm PMMA spheres (Figure 12).
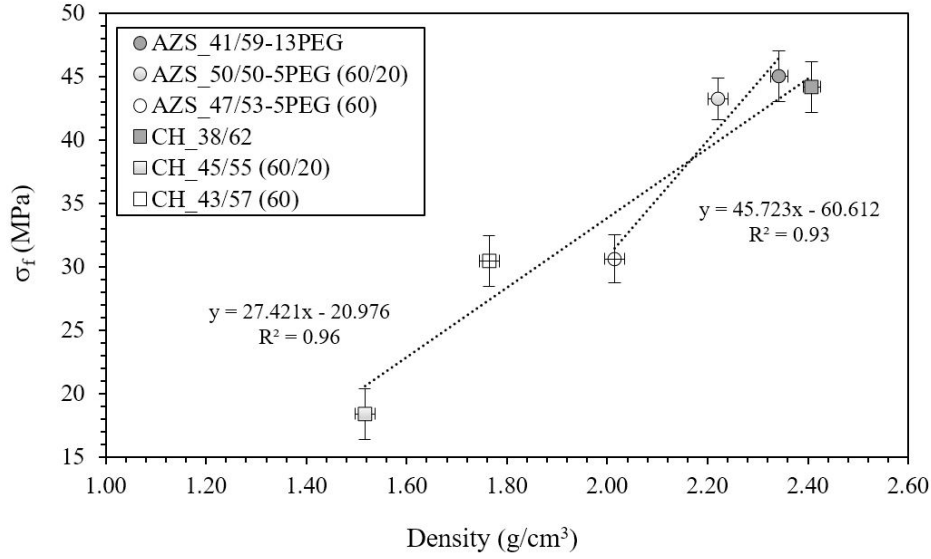
Figure 12: Bending strength vs. density of dense and porous AZS and CH 3D printed samples

Porosity and pores size distribution, as determined via mercury intrusion porosimetry (MIP), of dense and porous CH and AZS 3D-printed samples are reported in Figure 13a and Figure 13b, respectively, where porosity is divided in macropores (d >10 µm), mesopores (1 < d < 10 µm) and micropores (d < 1 µm).

CH_38/62 sample is characterized by approx. 15% porosity, mainly composed by mesopores (Figure 13a), and imputable to water loss [71]. However, just a moderate increase of the overall porosity was observed in the CH_43/57 (60) sample, due to the concomitant expected increase of macropores and decrease of mesopores. Conversely, CH_45/55 (60/20) samples present a porosity increase consistent with PMMA spheres volume addition. It is supposed that the overall porosity of CH_43/57 (60) was underestimated by MIP, probably due to a not complete Hg intrusion inside the isolated macropores, as highlighted in the microstructure depicted in Figure 17b (see section § 3.3).

AZS dense specimen (Figure 13b) contained a significant higher porosity amount (approx. 25%, mainly due to mesopores), as compared to CH. Such difference can be explained by considering both the slightly higher water amount in AZS (L/S of 41/59) than in CH (38/62), and above all the presence of 13 wt% PEG in AZS formulation, that is responsible of a further porosity increase after thermal treatment. Considering porous

AZS samples, porosity increase is coherent to the added volume of PMMA spheres (i.e. 30 vol%) and also the sharp increase of macropores (i.e. d > 10 µm) can be ascribed to PMMA spheres decomposition.
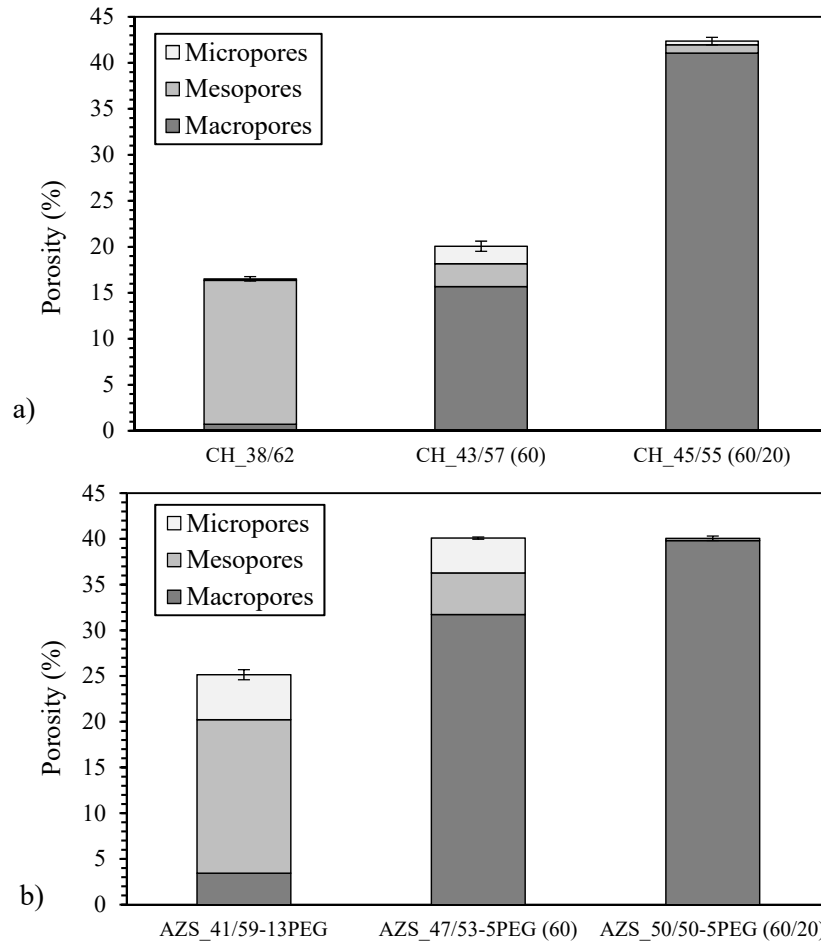

Figure 13: Open porosity and pores distribution of dense and porous a) CH and b) AZS 3D-printed samples

To better understand the influence of porosity on density and bending strength, Figure 14 reports the correlation between 3D-printed samples density and normalized bending strength (relatively to porosity as determined via MIP). Once again, a linear relationship exists between these parameters, highlighting their mutual influence. Higher differences are recognizable among CH samples compared to AZS ones probably due to the different microstructure as will be discussed in the following.
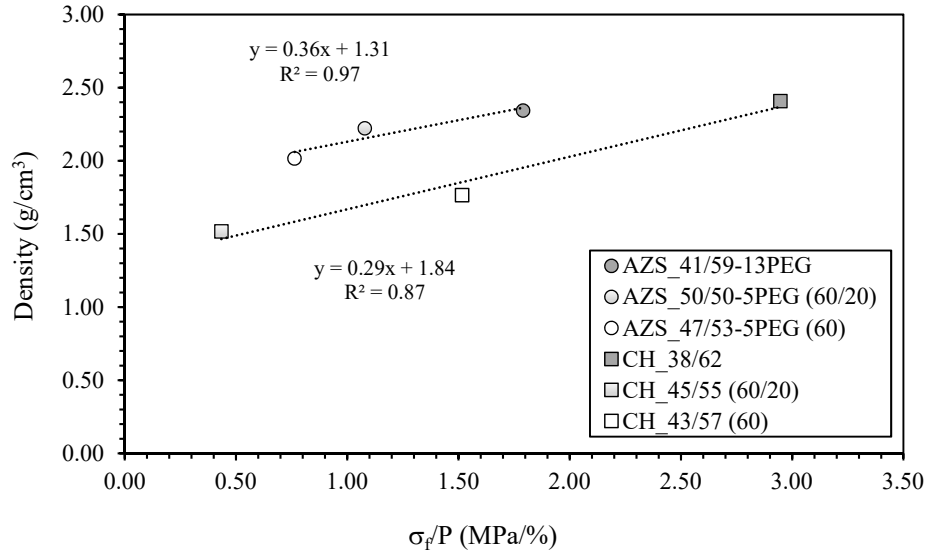
20

Figure 14: Correlation between density and normalized bending strength of dense and porous AZS and CH 3D-printed samples

3.3 Optical and FE-SEM analyses

After optimization of the alkali-activated pastes, in terms of printability, shape retention and PMMA spheres dispersion, lattice samples were successfully printed with the selected formulations, listed in the last column of Table 1. The difficulty in printing lattice structures is represented by the fabrication of geometries with suspended parts (i.e. the span between two struts of the inferior layer). Thus, pastes rheology is fundamental in order to be printable but also to be capable to withstand their own weight without deformation.

Three different lattice structures were printed (Figure 15a), having three different strut spans (1.25, 1.70 and 2.50 mm, for the 75, 50 and 25 % infill, respectively). No meaningful differences are recognizable between CAD models (Figure 4b) and printed lattice structures (Figure 15a), resulting in a successful printing. Deposited struts are well parallel each other and the effective pastes deposition is clearly recognizable since no struts are visible from the underneath layers (Figure 15b-d). The same considerations can be done for lattice samples added with PMMA beads, where the ability to print the suspended parts was proved again (Figure 15e).
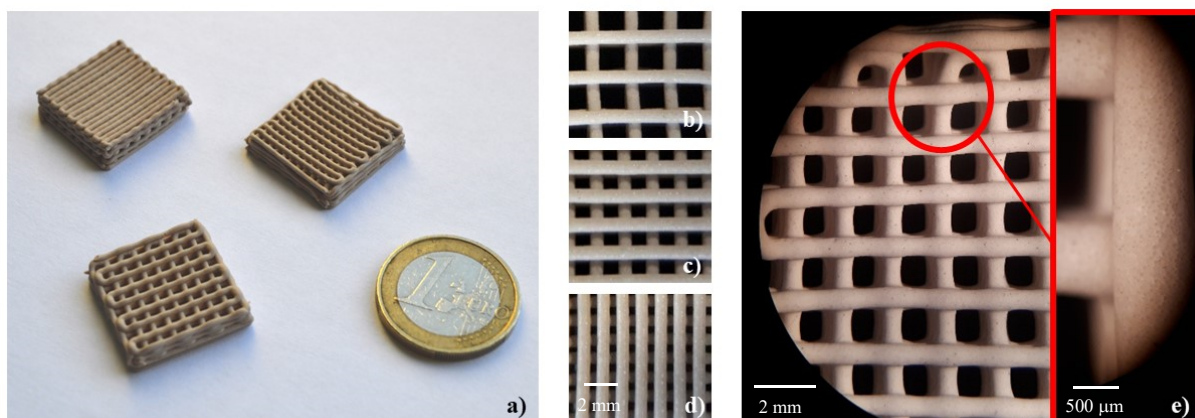
Figure 15: 3D-printed lattice structures: a) CH_38/62 with different infills, b) 25%, c) 50% and d) 75%, respectively; e) CH_43/57 (60) 50% infill and detail of the PMMA spheres within the filament

Representative FE-SEM micrographs of 3D-printed dense and porous lattice samples are reported in Figure 16. In particular, CH_38/62 deposited filaments regularity is clear in Figure 16a. On the contrary, in Figure 16b a single deposited filament cross section of a porous lattice structure of CH_45/55 (60/20) sample is presented. As evident, filaments cross section was perfectly circular, with a diameter of approx. 940 ± 20 μm (determined via image analysis), proving the good extrusion/deposition process. Filament diameter is higher than the nozzle one (i.e. 840 μm) due to the occurrence of the well-known die swell phenomenon (i.e. swelling of the extrudate out of the extruder die). Moreover, a good dispersion and distribution of pores in the filament cross section is also evident (Figure 16b). Pores, deriving from PMMA spheres decomposition, have a perfect spherical shape with diameters corresponding to the used PMMA spheres (i.e. 60 and 20 μm, respectively) (Figure 16c). Finally, an interconnection between pores is also recognizable in some cases (white arrows in Figure 16c).
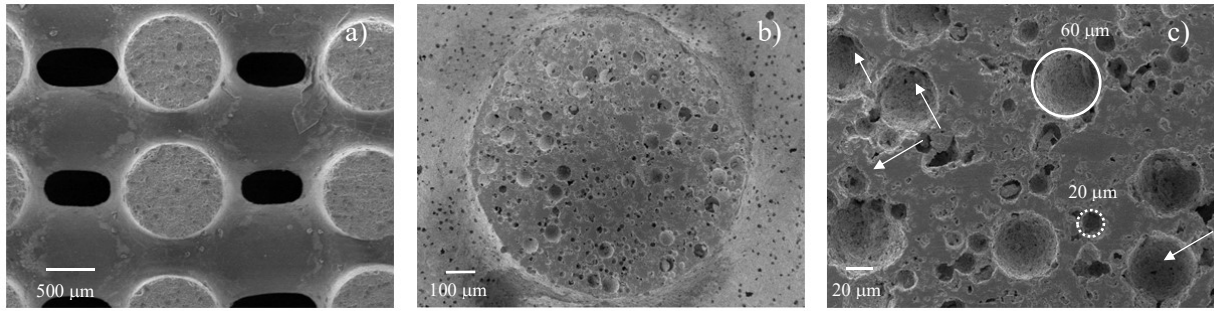
Figure 16: FE-SEM micrographs of lattice structure, a) CH_38/62, b) CH_45/55 (60/20) cross section of a single deposited filament and b) CH_45/55 (60/20) pores detail (white arrows indicate interconnected pores)

FE-SEM micrographs of CH and AZS prismatic samples cross section are reported in Figure 17 and Figure 18, respectively. Coherently to MIP results (Figure 13), AZS_41/59-13PEG sample (Figure 18a) is more porous than CH_38/62 ones (Figure 17a) due to PEG decomposition during thermal treatment. Conversely, CH presents a highly compact and homogeneous microstructure, with a limited and fine porosity, still in agreement with MIP data. In this material, the addition of the PMMA microspheres (60 μm diameter) produces almost spherical pores, embedded in a still highly compact microstructure. In the case of AZS microporous sample, we can observe a dual porosity: the spherical one, created by the PMMA decomposition, and the irregular ones in size and dimension, due to PEG decomposition. By comparing AZS_47/53-5PEG (60) and CH_43/57 (60) porous samples (Figure 17b and Figure 18b, respectively), the spherical pores deriving from PMMA decomposition are evident. Moreover, the lack of interconnection among pores is responsible of the slight porosity increase of CH_43/57 (60) samples compared to CH dense samples (Figure 13), as previously hypothesized. Finally, considering AZS_50/50-5PEG (60/20) and CH_45/55 (60/20) porous samples (Figure 18c and Figure 17c, respectively), a very high interconnected porous microstructure is clearly recognizable. Therefore, these microstructural differences are responsible of the different physical and mechanical properties.
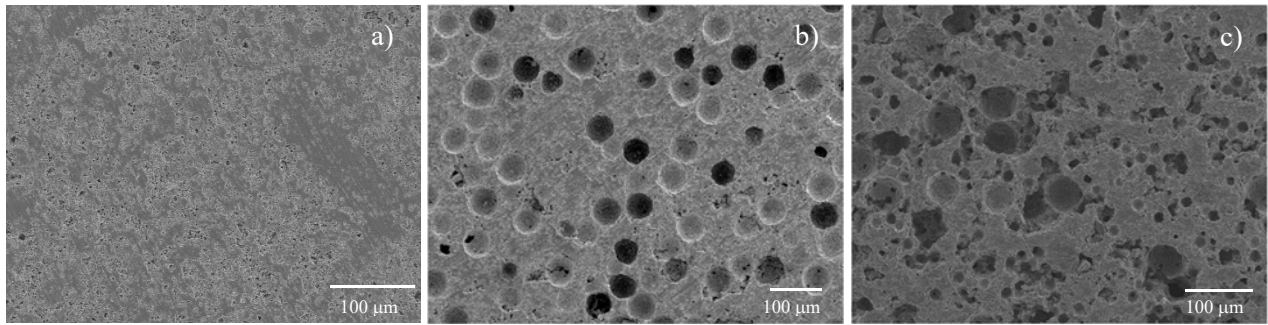
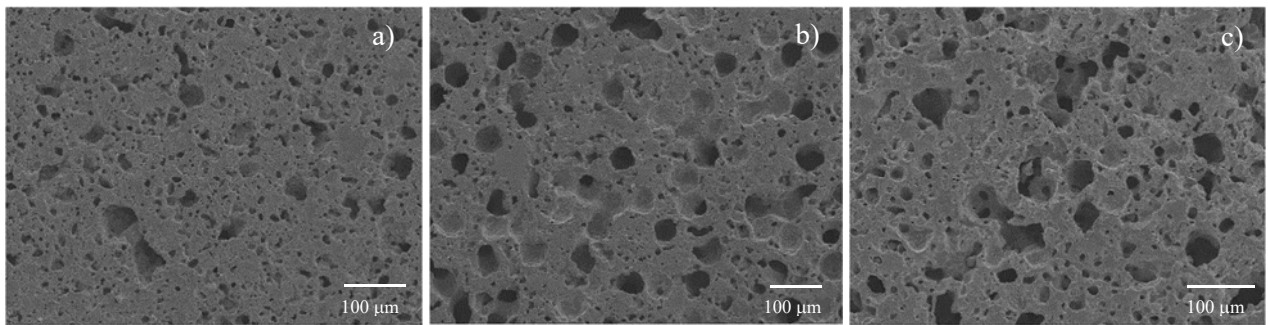**Figure 17:** CH prismatic samples cross section, a) CH_38/62, b) CH_43/57 (60) and c) CH_45/55 (60/20)

Figure 18: AZS prismatic samples cross section, a) AZS_41/59-13PEG, b) AZS_47/53-5PEG (60) and c) AZS_50/50-5PEG (60/20)

4. Conclusions

Direct Ink Writing (DIW) of alkali-activated pastes prepared using refractory wastes was investigated for the first time, and successfully achieved. Two different aluminosilicate wastes were used: chamotte (CH, mainly composed of corundum, mullite and andalusite) and alumina-zirconia-silica (AZS, composed by baddeleyite, corundum and amorphous silica). In particular, the ability of these refractory wastes-based alkali-activated pastes to well withstand high temperatures (as demonstrated in a previous work [71]) was exploited, to obtain 3D-printed samples with excellent mechanical properties. In fact, flexural strengths of approx. 45 MPa were obtained both for AZS and CH 3D-printed dense samples after a thermal treatment at 800 °C.

The successes of the 3D-printing process was mainly due to the optimization of the rheology of the fresh pastes: the best formulations were found to be those with a shear viscosity of approx. 200 Pa·s, and a printability range of both waste-based formulation was determined. The optimized formulations were used to print not only bulk samples, but also lattice structures, further highlighting the full control of the process. These lattice structures, with different infills and different strut spans (2.50, 1.70 and 1.25 mm, for the 25, 50

and 75% infill, respectively) were in fact correctly 3D-printed without any deformation of the deposited filament circular shape

Moreover, polymethyl methacrylate (PMMA) beads of different diameters (20 and 60 μm, respectively) were added to the formulations, to induce the formation of an additional porosity in both dense and lattice materials, leading – in this last case – to hierarchically porous samples. The results achieved in this work can be regarded as the starting point for future researches in which lattice porous structures can be further engineered for specific industrial applications (such as water and wastewater treatment, catalyst support, filtration membranes, etc.) in which customized, high-strength and in some case high-temperature stability structures are required.

Acknowledgments

References

1 Davidovits J. Geopolymers: ceramic-like inorganic polymers. J Ceram Sci Technol 2017;8:335–50. https://doi.org/10.4416/JCST2017-00038

2 Singh B, Ishwarya G, Gupta M, Bhattacharyya SK. Geopolymer concrete: A review of some recent developments. Constr Build Mater 2015;85:78–90. https://doi.org/10.1016/j.conbuildmat.2015.03.036

3 Provis JL, Palomo A, Shi C. Advances in understanding alkali-activated materials. Cem Concr Res 2015;78:110–25. https://doi.org/10.1016/j.cemconres.2015.04.013

4 Provis JL, Bernal SA. Geopolymers and related alkali-activated materials. Annu Rev Mater Res 2014;44:299–327. https://doi.org/10.1146/annurev-matsci-070813-113515

5 Coppola, L., Coffetti, D., Crotti, E., Gazzaniga, G., & Pastore, T. (2020). The Durability of One-Part Alkali-Activated Slag-Based Mortars in Different Environments. *Sustainability*, *12*(9), 3561. https://doi.org/10.3390/su12093561

6 El-Gamal, S. M. A., & Selim, F. A. (2017). Utilization of some industrial wastes for eco-friendly cement production. *Sustainable Materials and Technologies*, *12*, 9-17. https://doi.org/10.1016/j.susmat.2017.03.001

7 Luukkonen, T., Abdollahnejad, Z., Yliniemi, J., Mastali, M., Kinnunen, P., & Illikainen, M. (2019). Alkali-activated soapstone waste-Mechanical properties, durability, and economic prospects. *Sustainable Materials and Technologies*, *22*, e00118. https://doi.org/10.1016/j.susmat.2019.e00118

8 Silva, G., Kim, S., Aguilar, R., & Nakamatsu, J. (2020). Natural fibers as reinforcement additives for geopolymers–A review of potential eco-friendly applications to the construction industry. *Sustainable Materials and Technologies*, *23*, e00132. https://doi.org/10.1016/j.susmat.2019.e00132

9 Gao, H., Liu, H., Liao, L., Mei, L., Zhang, F., Zhang, L., ... & Lv, G. (2020). A bifunctional hierarchical porous kaolinite geopolymer with good performance in thermal and sound insulation. Construction and Building Materials, 251, 118888. https://doi.org/10.1016/j.conbuildmat.2020.118888

10 Gao, H., Liao, L., Liu, H., Mei, L., Wang, Z., Huang, D., ... & Wang, C. (2020). Optimization of thermal insulation performance of porous geopolymers under the guidance of thermal conductivity calculation. Ceramics International. https://doi.org/10.1016/j.ceramint.2020.03.221

11 Palmero, P., Formia, A., Antonaci, P., Brini, S., & Tulliani, J. M. (2015). Geopolymer technology for application-oriented dense and lightened materials. Elaboration and characterization. *Ceramics International*, *41*(10), 12967-12979. https://doi.org/10.1016/j.ceramint.2015.06.140

12 Roviello, G., Menna, C., Tarallo, O., Ricciotti, L., Messina, F., Ferone, C., ... & Cioffi, R. (2017). Lightweight geopolymer-based hybrid materials. *Composites Part B: Engineering*, *128*, 225-237. https://doi.org/10.1016/j.compositesb.2017.07.020

13 Petlitckaia, S., & Poulesquen, A. (2019). Design of lightweight metakaolin based geopolymer foamed with hydrogen peroxide. *Ceramics International*, *45*(1), 1322-1330. https://doi.org/10.1016/j.ceramint.2018.10.021

14 Shi, J., Liu, B., Liu, Y., Wang, E., He, Z., Xu, H., & Ren, X. (2020). Preparation and characterization of lightweight aggregate foamed geopolymer concretes aerated using hydrogen peroxide. *Construction and Building Materials*, *256*, 119442. https://doi.org/10.1016/j.conbuildmat.2020.119442

15 Ziegler, D.; Formia, A.; Tulliani, J.-M.; Palmero, P. Environmentally-Friendly Dense and Porous Geopolymers Using Fly Ash and Rice Husk Ash as Raw Materials. Materials 2016, 9, 466. https://doi.org/10.3390/ma9060466

16 Shuai, Q., Xu, Z., Yao, Z., Chen, X., Jiang, Z., Peng, X., ... & Li, H. (2020). Fire resistance of phosphoric acid-based geopolymer foams fabricated from metakaolin and hydrogen peroxide. Materials Letters, 263, 127228. https://doi.org/10.1016/j.matlet.2019.127228

17 Peng, X., Li, H., Shuai, Q., & Wang, L. (2020). Fire Resistance of Alkali Activated Geopolymer Foams Produced from Metakaolin and Na2O2. Materials, 13(3), 535. https://doi.org/10.3390/ma13030535

18 Peng, X., Shuai, Q., Li, H., Ding, Q., Gu, Y., Cheng, C., & Xu, Z. (2020). Fabrication and Fireproofing Performance of the Coal Fly Ash-Metakaolin-Based Geopolymer Foams. Materials, 13(7), 1750. https://doi.org/10.3390/ma13071750

19 Luukkonen, T., Heponiemi, A., Runtti, H. et al. Application of alkali-activated materials for water and wastewater treatment: a review. Rev Environ Sci Biotechnol 18, 271–297 (2019). https://doi.org/10.1007/s11157-019-09494-0

20 Bumanis, G., Novais, R. M., Carvalheiras, J., Bajare, D., & Labrincha, J. A. (2019). Metals removal from aqueous solutions by tailored porous waste-based granulated alkali-activated materials. Applied Clay Science, 179, 105147. https://doi.org/10.1016/j.clay.2019.105147

21 Tan, T. H., Mo, K. H., Ling, T. C., & Lai, S. H. (2020). Current development of geopolymer as alternative adsorbent for heavy metal removal. Environmental Technology & Innovation, 100684. https://doi.org/10.1016/j.eti.2020.100684

22 Onutai, S., Kobayashi, T., Thavorniti, P., & Jiemsirilers, S. (2019). Porous fly ash-based geopolymer composite fiber as an adsorbent for removal of heavy metal ions from wastewater. Materials Letters, 236, 30-33. https://doi.org/10.1016/j.matlet.2018.10.035

23 Chen, H., Zhang, Y. J., He, P. Y., Li, C. J., & Li, H. (2020). Coupling of self-supporting geopolymer membrane with intercepted Cr (III) for dye wastewater treatment by hybrid photocatalysis and membrane separation. Applied Surface Science, 146024. https://doi.org/10.1016/j.apsusc.2020.146024

24 Innocentini, M. D., Botti, R. F., Bassi, P. M., Paschoalato, C. F., Flumignan, D. L., Franchin, G., & Colombo, P. (2019). Lattice-shaped geopolymer catalyst for biodiesel synthesis fabricated by additive manufacturing. Ceramics International, 45(1), 1443-1446. https://doi.org/10.1016/j.ceramint.2018.09.239

25 Zhang, Y. J., Han, Z. C., He, P. Y., & Chen, H. (2020). Geopolymer-based catalysts for cost-effective environmental governance: A review based on source control and end-of-pipe treatment. Journal of Cleaner Production, 121556. https://doi.org/10.1016/j.jclepro.2020.121556

26 Asim, N., Alghoul, M., Mohammad, M., Amin, M. H., Akhtaruzzaman, M., Amin, N., & Sopian, K. (2019). Emerging sustainable solutions for depollution: geopolymers. Construction and Building Materials, 199, 540-548. https://doi.org/10.1016/j.conbuildmat.2018.12.043

27 Wang, J. T., Ge, Y. Y., He, Y., Xu, M. X., & Cui, X. M. (2019). A porous gradient geopolymer-based tube membrane with high PM removal rate for air pollution. Journal of cleaner production, 217, 335-343. https://doi.org/10.1016/j.jclepro.2019.01.268

28 Papa, E., Mor, M., Murri, A. N., Landi, E., & Medri, V. (2020). Ice-templated geopolymer beads for dye removal. Journal of Colloid and Interface Science. https://doi.org/10.1016/j.jcis.2020.03.104

29 Szechyńska-Hebda, M., Marczyk, J., Ziejewska, C., Hordyńska, N., Mikuła, J., & Hebda, M. (2019). Optimal design of pH-neutral geopolymer foams for their use in ecological plant cultivation systems. Materials, 12(18), 2999. https://doi.org/10.3390/ma12182999

30 Bai, C., & Colombo, P. (2018). Processing, properties and applications of highly porous geopolymers: A review. Ceramics International, 44(14), 16103-16118. https://doi.org/10.1016/j.ceramint.2018.05.219

31 Novais, R. M., Pullar, R. C., & Labrincha, J. A. (2019). Geopolymer foams: an overview of recent advancements. Progress in Materials Science, 100621. https://doi.org/10.1016/j.pmatsci.2019.100621

32 Bai, C., & Colombo, P. (2017). High-porosity geopolymer membrane supports by peroxide route with the addition of egg white as surfactant. Ceramics International, 43(2), 2267-2273. https://doi.org/10.1016/j.ceramint.2016.10.205

33 Bai, C., Ni, T., Wang, Q., Li, H., & Colombo, P. (2018). Porosity, mechanical and insulating properties of geopolymer foams using vegetable oil as the stabilizing agent. Journal of the European Ceramic Society, 38(2), 799-805. https://doi.org/10.1016/j.jeurceramsoc.2017.09.021

34 Bai, C., Zheng, J., Rizzi, G. A., & Colombo, P. (2018). Low-temperature fabrication of SiC/geopolymer cellular composites. Composites Part B: Engineering, 137, 23-30. https://doi.org/10.1016/j.compositesb.2017.11.013

35 Phavongkham, V., Wattanasiriwech, S., Cheng, T. W., & Wattanasiriwech, D. (2020). Effects of surfactant on thermo-mechanical behavior of geopolymer foam paste made with sodium perborate foaming agent. Construction and Building Materials, 243, 118282. https://doi.org/10.1016/j.conbuildmat.2020.118282

36 Masi, G., Rickard, W. D., Vickers, L., Bignozzi, M. C., & Van Riessen, A. (2014). A comparison between different foaming methods for the synthesis of light weight geopolymers. Ceramics International, 40(9), 13891-13902. https://doi.org/10.1016/j.ceramint.2014.05.108

37 Tulliani, J. M., Lombardi, M., Palmero, P., Fornabaio, M., & Gibson, L. J. (2013). Development and mechanical characterization of novel ceramic foams fabricated by gel-casting. *Journal of the European Ceramic Society*, *33*(9), 1567-1576. https://doi.org/10.1016/j.jeurceramsoc.2013.01.038

38 Tulliani, J. M., Bartuli, C., Bemporad, E., Naglieri, V., & Sebastiani, M. (2009). Preparation and mechanical characterization of dense and porous zirconia produced by gel casting with gelatin as a gelling agent. *Ceramics International*, *35*(6), 2481-2491. https://doi.org/10.1016/j.ceramint.2009.02.017

39 Liu, J., Yang, H., Ren, B., Rong, Y., Xi, X., Lu, Y., ... & Yang, J. (2020). Highly porous ZrO2 cellular ceramics with 3D network architecture. Ceramics International, 46(6), 7149-7154. https://doi.org/10.1016/j.ceramint.2019.11.207

40 Montanaro, L., Coppola, B., Palmero, P., & Tulliani, J. M. (2019). A review on aqueous gelcasting: A versatile and low-toxic technique to shape ceramics. Ceramics International, 45(7), 9653-9673. https://doi.org/10.1016/j.ceramint.2018.12.079

41 Scotti, K. L., & Dunand, D. C. (2018). Freeze casting–A review of processing, microstructure and properties via the open data repository, FreezeCasting. net. *Progress in Materials Science*, *94*, 243-305. https://doi.org/10.1016/j.pmatsci.2018.01.001

42 Liao, Y., Liu, C., Coppola, B., Barra, G., Di Maio, L., Incarnato, L., & Lafdi, K. (2019). Effect of porosity and crystallinity on 3D printed PLA properties. *Polymers*, *11*(9), 1487. https://doi.org/10.3390/polym11091487

43 Coppola, B., Cappetti, N., Di Maio, L., Scarfato, P., & Incarnato, L. (2018). 3D printing of PLA/clay nanocomposites: influence of printing temperature on printed samples properties. *Materials*, *11*(10), 1947. https://doi.org/10.3390/ma11101947

44 Ngo, T. D., Kashani, A., Imbalzano, G., Nguyen, K. T., & Hui, D. (2018). Additive manufacturing (3D printing): A review of materials, methods, applications and challenges. *Composites Part B: Engineering*, *143*, 172-196. https://doi.org/10.1016/j.compositesb.2018.02.012

45 Xia, M., Nematollahi, B., & Sanjayan, J. (2019). Printability, accuracy and strength of geopolymer made using powder-based 3D printing for construction applications. *Automation in Construction*, *101*, 179-189. https://doi.org/10.1016/j.autcon.2019.01.013

46 Mostafaei, A., Elliott, A. M., Barnes, J. E., Cramer, C. L., Nandwana, P., & Chmielus, M. (2020). Binder jet 3D printing–process parameters, materials, properties, and challenges. *Progress in Materials Science*, 100684. https://doi.org/10.1016/j.pmatsci.2020.100684

47 Nematollahi, B., Xia, M., & Sanjayan, J. (2019). Enhancing Strength of Powder-Based 3D Printed Geopolymers for Digital Construction Applications. In *Rheology and Processing of Construction Materials* (pp. 417-425). Springer, Cham. https://doi.org/10.1007/978-3-030-22566-7_48

48 Xia, M., & Sanjayan, J. (2016). Method of formulating geopolymer for 3D printing for construction applications. *Materials & Design*, *110*, 382-390. https://doi.org/10.1016/j.matdes.2016.07.136

49 Cesaretti, G., Dini, E., De Kestelier, X., Colla, V., & Pambaguian, L. (2014). Building components for an outpost on the Lunar soil by means of a novel 3D printing technology. *Acta Astronautica*, *93*, 430-450. https://doi.org/10.1016/j.actaastro.2013.07.034

50 Albar, A., Chougan, M., Al-Kheetan, M. J., Swash, M. R., & Ghaffar, S. H. (2020). Effective extrusion-based 3D printing system design for cementitious-based materials. Results in Engineering, 100135. https://doi.org/10.1016/j.rineng.2020.100135

51 Panda, B., & Tan, M. J. (2018). Experimental study on mix proportion and fresh properties of fly ash based geopolymer for 3D concrete printing. Ceramics International, 44(9), 10258-10265. https://doi.org/10.1016/j.ceramint.2018.03.031

52 Agnoli, E., Ciapponi, R., Levi, M., & Turri, S. (2019). Additive Manufacturing of Geopolymers Modified with Microalgal Biomass Biofiller from Wastewater Treatment Plants. Materials, 12(7), 1004. https://doi.org/10.3390/ma12071004

53 Panda, B., Paul, S. C., Hui, L. J., Tay, Y. W. D., & Tan, M. J. (2017). Additive manufacturing of geopolymer for sustainable built environment. Journal of cleaner production, 167, 281-288. https://doi.org/10.1016/j.jclepro.2017.08.165

54 Panda, B., Paul, S. C., Mohamed, N. A. N., Tay, Y. W. D., & Tan, M. J. (2018). Measurement of tensile bond strength of 3D printed geopolymer mortar. Measurement, 113, 108-116. https://doi.org/10.1016/j.measurement.2017.08.051

55 Panda, B., Unluer, C., & Tan, M. J. (2018). Investigation of the rheology and strength of geopolymer mixtures for extrusion-based 3D printing. Cement and Concrete Composites, 94, 307-314. https://doi.org/10.1016/j.cemconcomp.2018.10.002

56 Sun, C., Xiang, J., Xu, M., He, Y., Tong, Z., & Cui, X. (2020). 3D extrusion free forming of geopolymer composites: Materials modification and processing optimization. Journal of Cleaner Production, 120986. https://doi.org/10.1016/j.jclepro.2020.120986

57 Chougan, M., Ghaffar, S. H., Jahanzat, M., Albar, A., Mujaddedi, N., & Swash, R. (2020). The influence of nano-additives in strengthening mechanical performance of 3D printed multi-binder geopolymer composites. Construction and Building Materials, 250, 118928. https://doi.org/10.1016/j.conbuildmat.2020.118928

58 Alghamdi, H., Nair, S. A., & Neithalath, N. (2019). Insights into material design, extrusion rheology, and properties of 3D-printable alkali-activated fly ash-based binders. Materials & Design, 167, 107634. https://doi.org/10.1016/j.matdes.2019.107634

59 Panda, B., Ruan, S., Unluer, C., & Tan, M. J. (2019). Improving the 3D printability of high volume fly ash mixtures via the use of nano attapulgite clay. Composites Part B: Engineering, 165, 75-83. https://doi.org/10.1016/j.compositesb.2018.11.109

60 Li, Z., Wang, L., & Ma, G. (2020). Mechanical improvement of continuous steel microcable reinforced geopolymer composites for 3D printing subjected to different loading conditions. Composites Part B: Engineering, 187, 107796. https://doi.org/10.1016/j.compositesb.2020.107796

61 Lim, J. H., Panda, B., & Pham, Q. C. (2018). Improving flexural characteristics of 3D printed geopolymer composites with in-process steel cable reinforcement. Construction and Building Materials, 178, 32-41. https://doi.org/10.1016/j.conbuildmat.2018.05.010

62 Bong, S. H., Nematollahi, B., Nazari, A., Xia, M., & Sanjayan, J. (2019). Method of optimisation for ambient temperature cured sustainable geopolymers for 3D printing construction applications. Materials, 12(6), 902. https://doi.org/10.3390/ma12060902

63 Panda, B., Unluer, C., & Tan, M. J. (2019). Extrusion and rheology characterization of geopolymer nanocomposites used in 3D printing. Composites Part B: Engineering, 176, 107290. https://doi.org/10.1016/j.compositesb.2019.107290

64 Franchin, G., Scanferla, P., Zeffiro, L., Elsayed, H., Baliello, A., Giacomello, G., ... & Colombo, P. (2017). Direct ink writing of geopolymeric inks. Journal of the European Ceramic Society, 37(6), 2481-2489. https://doi.org/10.1016/j.jeurceramsoc.2017.01.030

65 Alghamdi, H., & Neithalath, N. (2019). Synthesis and characterization of 3D-printable geopolymeric foams for thermally efficient building envelope materials. Cement and Concrete Composites, 104, 103377. https://doi.org/10.1016/j.cemconcomp.2019.103377

66 Coppola, B., Palmero, P., Montanaro, L., & Tulliani, J. M. (2019). Alkali-activation of marble sludge: Influence of curing conditions and waste glass addition. *Journal of the European Ceramic Society, 40,* 3776-3787. https://doi.org/10.1016/j.jeurceramsoc.2019.11.068

67 P. Palmero, A. Formia, J.M. Tulliani, P. Antonaci, Valorisation of alumino-silicate stone muds: From wastes to source materials for innovative alkali-activated materials, Cem. Concr. Compos., 83 (2017) 251-262. https://doi.org/10.1016/j.cemconcomp.2017.07.011

68 Coppola, B., Tulliani, J. M., Antonaci, P., & Palmero, P. (2020). Role of Natural Stone Wastes and Minerals in the Alkali Activation Process: A Review. *Materials*, *13*(10), 2284. https://doi.org/10.3390/ma13102284

69 Bassani, M., Tefa, L., Russo, A., & Palmero, P. (2019). Alkali-activation of recycled construction and demolition waste aggregate with no added binder. *Construction and Building Materials*, *205*, 398-413. https://doi.org/10.1016/j.conbuildmat.2019.02.031

70 Bassani, M., Tefa, L., Coppola, B., & Palmero, P. (2019). Alkali-activation of aggregate fines from construction and demolition waste: Valorisation in view of road pavement subbase applications. *Journal of Cleaner Production*, *234*, 71-84. https://doi.org/10.1016/j.jclepro.2019.06.207

71 Coppola, B., Tardivat, C., Richaud, S., Tulliani, J. M., Montanaro, L., & Palmero, P. (2020). Alkali-activated refractory wastes exposed to high temperatures: development and characterization. *Journal of the European Ceramic Society*, 40, 3314-3326 https://doi.org/10.1016/j.jeurceramsoc.2020.02.052

72 M'barki, A., Bocquet, L., Stevenson, A. (2017). Linking rheology and printability for dense and strong ceramics by direct ink writing. Scientific reports, 7(1), 1-10. https://doi.org/10.1038/s41598-017-06115-0

73 Fateh, T., Richard, F., Rogaume, T., & Joseph, P. (2016). Experimental and modelling studies on the kinetics and mechanisms of thermal degradation of polymethyl methacrylate in nitrogen and air. *Journal of Analytical and Applied Pyrolysis*, *120*, 423-433. https://doi.org/10.1016/j.jaap.2016.06.014

74 Coppola, B., Di Maio, L., Scarfato, P., & Incarnato, L. (2015, December). Use of polypropylene fibers coated with nano-silica particles into a cementitious mortar. In AIP Conference Proceedings (Vol. 1695, No. 1, p. 020056). AIP Publishing. https://doi.org/10.1063/1.4937334

75 Ferrara, G., Coppola, B., Di Maio, L., Incarnato, L., & Martinelli, E. (2019). Tensile strength of flax fabrics to be used as reinforcement in cement-based composites: experimental tests under different environmental exposures. Composites Part B: Engineering, 168, 511-523. https://doi.org/10.1016/j.compositesb.2019.03.062